

Mimicking the Intradiol Catechol Cleavage Activity of Catechol Dioxygenase by High-Spin Iron(III) Complexes of a New Class of a Facially Bound [N₂O] Ligand

Manas K. Panda,[†] Alex John,[†] Mobin M. Shaikh,[‡] and Prasenjit Ghosh^{*†}

Department of Chemistry and National Single Crystal X-ray Diffraction Facility, Indian Institute of Technology Bombay, Powai, Mumbai 400 076, India

Received August 19, 2008

A series of high-spin iron(III) complexes, {*N*-*R*-2-[(pyridin-2-ylmethyl)amino]acetamide}FeCl₃ [*R* = mesityl (**1b**), 2,6-Et₂C₆H₃ (**2b**), and 2,6-*i*-Pr₂C₆H₃ (**3b**)], that functionally emulate the intradiol catechol dioxygenase enzyme are reported. In particular, these enzyme mimics, **1b**, **2b**, and **3b**, which utilized molecular oxygen in carrying out the intradiol catechol cleavage of 3,5-di-*tert*-butylcatechol with high regioselectivity (ca. 81–85%) at room temperature under ambient conditions, were designed by employing a new class of a facially bound [N₂O] ligand, namely, *N*-*R*-2-[(pyridin-2-ylmethyl)amino]acetamide [*R* = mesityl (**1a**), 2,6-Et₂C₆H₃ (**2a**), and 2,6-*i*-Pr₂C₆H₃ (**3a**)]. The density functional theory studies revealed that the intradiol catechol cleavage reaction proceeded by an iron(III) peroxo intermediate that underwent 1,2-Criegee rearrangement to yield the intradiol catechol cleaved products analogous to the native enzyme.

Introduction

Pseudomonas, a kind of soil bacteria, possesses a unique and remarkable metabolic ability not only to degrade aromatic compounds but also to utilize them as the sole carbon source for their growth.^{1,2} Not surprisingly, this obscure bacterium has triggered intense research over the last few decades particularly because of its relevance in reducing many aromatic pollutants in the environment.³ A key step in the aromatic degradation pathway involves oxidative cleavage of catechols or substituted catechols to

yield acyclic compounds and is facilitated by a class of enzymes known as catechol dioxygenase. The oxidative cleavage of catechols represents the last step of the biodegradation of aromatic molecules in the environment.⁴ These enzymes carry out oxidative cleavage of the aromatic double bonds with the aid of molecular oxygen by inserting two O atoms of the dioxygen molecule in the acyclic product, and depending upon the site of the aromatic bond fissure relative to the hydroxyl groups in catechol, they are classified as either an intradiol⁵ or an extradiol⁶ cleavage enzyme.³ Quite interestingly, as a consequence of operating by mutually exclusive mechanistic pathways, these two enzymes give highly selective intradiol- or extradiol-cleaved products even though operating on a common catechol substrate.⁷

The necessary impetus for studying enzyme-catalyzed reactions like that of intradiol or extradiol catechol cleavage by catechol dioxygenase primarily arises from the fact that on many occasions there may exist very little or no precedence for such reactions in laboratory chemistry. Small-molecule modeling studies have played a pivotal role in

* To whom correspondence should be addressed. E-mail: pghosh@chem.iitb.ac.in. Fax: +91-22-2572-3480.

[†] Department of Chemistry.

[‡] National Single Crystal X-ray Diffraction Facility.

- (1) (a) Lange, S. J.; Que, L., Jr *Curr. Opin. Chem. Biol.* **1998**, *2*, 159–172. (b) Powlowski, J.; Shingler, V. *Biodegradation* **1994**, *5*, 219–236. (c) Williams, P. A.; Sayers, J. R. *Biodegradation* **1994**, *5*, 195–217. (d) Lipscomb, J. D.; Orville, A. M. In *Metal Ions in Biological Systems*; Sigel, H., Sigel, A., Eds.; Marcel Dekker: New York, 1992; Vol. 28, pp 243–298. (e) *Microbial Degradation of Organic Compounds*; Gibson, D. T., Ed.; Marcel Dekker: New York, 1984.
- (2) Mars, A. E.; Kingma, J.; Kaschabek, S. R.; Reinkee, W.; Janssen, D. B. *J. Bacteriol.* **1999**, *181*, 1309–1318.
- (3) (a) Costas, M.; Mehn, M. P.; Jensen, M. P.; Que, L., Jr *Chem. Rev.* **2004**, *104*, 939–986. (b) Solomon, E. I.; Decker, A.; Lehnert, N. *Proc. Natl. Acad. Sci. U.S.A.* **2003**, *100*, 3589–3594. (c) Solomon, E. I.; Brunold, T. C.; Davis, M. I.; Kemsley, J. N.; Lee, S.; Lehnert, N.; Neese, F.; Skulan, A. J.; Yang, Y.; Zhou, J. *Chem. Rev.* **2000**, *100*, 235–349. (d) Que, L., Jr.; Ho, R. Y. N. *Chem. Rev.* **1996**, *96*, 2607–2624.

(4) Bugg, T. D. H.; Winfield, C. J. *Nat. Prod. Rep.* **1998**, *5*, 513–530.

(5) Hayaishi, O.; Katagiri, M.; Rothberg, S. *J. Am. Chem. Soc.* **1955**, *77*, 5450–5451.

(6) Kojima, Y.; Itada, N.; Hayaishi, O. *J. Biol. Chem.* **1961**, *236*, 2223–2228.

(7) Bugg, T. D. H.; Lin, G. *Chem. Commun.* **2001**, 941–2.

understanding the enzyme mode of action, particularly in elucidating the role of the metal center in partaking such a selective cleavage of catechol substrates and, in this regard, the pioneering work by Funabiki,⁸ Que,⁹ Palaniandavar,¹⁰ Krebs¹¹ and others¹² deserves special mention. What emerges from a careful scrutiny of the small-molecule synthetic analogues that exist in the literature is that facially bound ligands with N/O donor sites are ideally suited for designing these model complexes.¹³ Apart from the binding preferences of the ligands, the Lewis acidity of the metal center was found to exercise a profound influence on the functional properties of these model complexes.¹³ Not surprisingly, the high-spin iron(III) complexes stabilized over facially bound [N_xO_y] ligands were found to best emulate the enzyme both structurally and functionally.^{9e,h,10d,f,12b,e}

With one of our aims being the design and synthesis of small-molecule metal complexes for their utility in biomedical applications that span from anticancer to antimicrobial

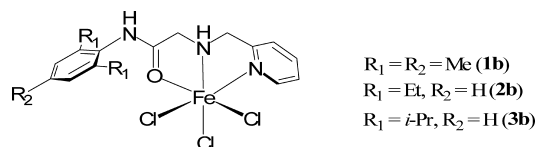


Figure 1

studies¹⁴ to the design of small-molecule synthetic mimics of enzyme active sites,¹⁵ we became interested in designing synthetic analogues of catechol dioxygenase. In particular, we set out to synthesize high-spin iron(III) complexes of a new class of a facially chelating [N₂O] ligand containing pyridyl N-donor, amine N-donor, and amide O-donor moieties. Here in this contribution we report a series of high-spin iron(III) complexes, {*N*-R-2-[(pyridin-2-ylmethyl)amino]acetamide}FeCl₃ [R = mesityl (**1b**), 2,6-Et₂C₆H₃ (**2b**) and 2,6-*i*-Pr₂C₆H₃ (**3b**)], that serve as excellent models for intradiol catechol dioxygenase by carrying out oxidative cleavage of 3,5-di-*tert*-butylcatechol using molecular oxygen at room temperature under ambient conditions and displaying high regioselectivity with respect to the intradiol-cleaved products (ca. 81–85%) similar to that of the native enzyme (Figure 1). Furthermore, the density functional theory (DFT) studies suggest that the **1b**, **2b**, and **3b** complexes perform catechol cleavage using molecular oxygen via an iron(III) peroxo intermediate similar to that reported in the case of the native enzyme.

Results and Discussion

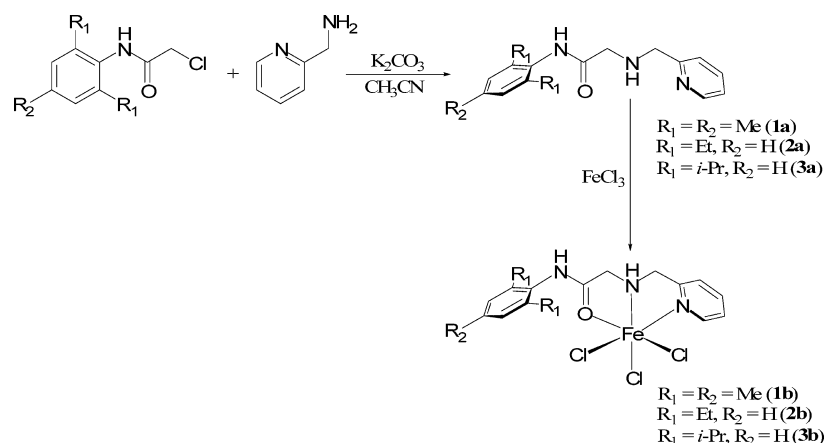
In keeping with the facial binding of the ligand, a new set of [N₂O]-type ligands, namely, *N*-R-2-[(pyridin-2-ylmethyl)amino]acetamide [R = mesityl (**1a**), 2,6-Et₂C₆H₃ (**2a**) and 2,6-*i*-Pr₂C₆H₃ (**3a**)], having pyridyl N-donor, amine N-donor, and amido O-donor moieties were designed for stabilizing the targeted synthetic analogues of catechol dioxygenase (Figure 1). Specifically, the **1a**, **2a**, and **3a** ligands were synthesized from the reaction of 2-chloro-*N*-(R)acetamide (R = mesityl, 2,6-Et₂C₆H₃ and 2,6-*i*-Pr₂C₆H₃) with 2-picoylamine in the presence of K₂CO₃ as a base (Scheme 1). The formation of **1a**, **2a**, and **3a** was evident from their ¹H NMR spectra, which showed two distinctive bridging methylene peaks (–CH₂–) appearing as singlets at ca. 4.00 and 3.50 ppm. The reaction of **1a**, **2a**, and **3a** with anhydrous FeCl₃ yielded the desired high-spin iron(III) complexes **1b**, **2b**, and **3b** in ca. 76–89% yield (Scheme 1).

The electronic spectra of the **1b**, **2b**, and **3b** complexes in CH₃CN showed two charge-transfer absorption bands, one centered on ~370 nm and the other at ~295 nm, similar to that observed in other high-spin octahedral iron(III) complexes (see Table S1 in the Supporting Information). For example, the octahedral iron(III) complex [bis(pyridin-2-ylmethyl)amine]FeCl₃¹⁶ showed similar charge-transfer bands at 400 nm ($\epsilon = 430 \text{ M}^{-1} \text{ cm}^{-1}$) and 352 nm ($\epsilon = 830 \text{ M}^{-1} \text{ cm}^{-1}$), while another high-spin iron(III) complex, namely,

- (8) (a) Higuchi, M.; Hitomi, Y.; Minami, H.; Tanaka, T.; Funabiki, T. *Inorg. Chem.* **2005**, *44*, 8810–8821. (b) Funabiki, T.; Mizoguchi, A.; Sugimoto, T.; Tada, S.; Tsuji, M.; Sakamoto, H.; Yoshida, S. *J. Am. Chem. Soc.* **1986**, *108*, 2921–2932. (c) Funabiki, T.; Sakamoto, H.; Yoshida, S.; Tarama, K. *J. Chem. Soc., Chem. Commun.* **1979**, 754–755.
- (9) (a) Jo, D.; Chiou, Y.; Que, L., Jr *Inorg. Chem.* **2001**, *40*, 3181–3190. (b) Jo, D.; Que, L., Jr *Angew. Chem., Int. Ed.* **2000**, *39*, 4284–4287. (c) Jang, H. G.; Cox, D. D.; Que, L., Jr *J. Am. Chem. Soc.* **1991**, *113*, 9200–9204. (d) Pyrz, J. W.; Pan, X.; Britton, D.; Que, L., Jr *Inorg. Chem.* **1991**, *30*, 3461–3464. (e) Cox, D. D.; Que, L., Jr *J. Am. Chem. Soc.* **1988**, *110*, 8085–8092. (f) Cox, D. D.; Benkovic, S. J.; Bloom, L. M.; Bradley, F. C.; Nelson, M. J.; Que, L., Jr.; Wallick, D. E. *J. Am. Chem. Soc.* **1988**, *110*, 2026–2032. (g) Que, L., Jr.; Lauffer, R. B.; Lynch, J. B.; Murch, B. P.; Pyrz, J. W. *J. Am. Chem. Soc.* **1987**, *109*, 5381–5385. (h) Que, L., Jr.; Kolanczyk, R. C.; White, L. S. *J. Am. Chem. Soc.* **1987**, *109*, 5373–5380. (i) White, L. S.; Nilsson, P. V.; Pignolet, L. H.; Que, L., Jr *J. Am. Chem. Soc.* **1984**, *106*, 8312–8313. (j) Heistand, R. H., II; Lauffer, R. B.; Fikrig, E.; Que, L., Jr *J. Am. Chem. Soc.* **1982**, *104*, 2789–2796. (k) Heistand, R. H., II; Roe, A. L.; Que, L., Jr *Inorg. Chem.* **1982**, *21*, 676–681.
- (10) (a) Visvaganesan, K.; Mayilmurugan, R.; Suresh, E.; Palaniandavar, M. *Inorg. Chem.* **2007**, *46*, 10294–10306. (b) Mayilmurugan, R.; Suresh, E.; Palaniandavar, M. *Inorg. Chem.* **2007**, *46*, 6038–6049. (c) Dhanalakshmi, T.; Bhuvaneshwari, M.; Palaniandavar, M. *J. Inorg. Biochem.* **2006**, *100*, 1527–1534. (d) Velusamy, M.; Mayilmurugan, R.; Palaniandavar, M. *J. Inorg. Biochem.* **2005**, *99*, 1032–1042. (e) Velusamy, M.; Mayilmurugan, R.; Palaniandavar, M. *Inorg. Chem.* **2004**, *43*, 6284–6293. (f) Velusamy, M.; Palaniandavar, M.; Gopalan, R. S.; Kulkarni, G. U. *Inorg. Chem.* **2003**, *42*, 8283–8293. (g) Viswanathan, R.; Palaniandavar, M.; Balasubramanian, T.; Muthiah, T. P. *Inorg. Chem.* **1998**, *37*, 2943–2951. (h) Viswanathan, R.; Palaniandavar, M. *J. Chem. Soc., Dalton Trans.* **1995**, 1259–1266.
- (11) (a) Xu, J.; Astner, J.; Walter, O.; Heinemann, F. W.; Schindler, S.; Merkel, M.; Krebs, B. *Eur. J. Inorg. Chem.* **2006**, 1601–1610. (b) Merkel, M.; Pascaly, M.; Krebs, B.; Astner, J.; Foxon, S. P.; Schindler, S. *Inorg. Chem.* **2005**, *44*, 7582–7589. (c) Pascaly, M.; Duda, M.; Schweppe, F.; Zurlinden, K.; Muller, F. K.; Krebs, B. *J. Chem. Soc., Dalton Trans.* **2001**, 828–837. (d) Duda, M.; Pascaly, M.; Krebs, B. *J. Chem. Soc., Chem. Commun.* **1997**, 835–836.
- (12) (a) Li, F.; Wang, M.; Li, P.; Zhang, T.; Sun, L. *Inorg. Chem.* **2007**, *46*, 9364–9371. (b) Bruijninx, P. C. A.; Lutz, M.; Spek, A. L.; Hagen, W. R.; van Koten, G.; Gebbink, R. J. M. *Inorg. Chem.* **2007**, *46*, 8391–8402. (c) Kaizer, J.; Zsigmond, Z.; Ganszky, I.; Speier, G.; Giorgi, M.; Reglier, M. *Inorg. Chem.* **2007**, *46*, 4660–4666. (d) Wang, C.; Lu, J.; Wei, H.; Takeda, M. *Inorg. Chim. Acta* **2007**, *360*, 2944–2952. (e) Bruijninx, P. C. A.; Lutz, M.; Spek, A. L.; Hagen, W. R.; Weckhuysen, B. M.; van Koten, G.; Gebbink, R. J. M. *J. Am. Chem. Soc.* **2007**, *129*, 2275–2286. (f) Fujii, H.; Funahashi, Y. *Angew. Chem., Int. Ed.* **2002**, *41*, 3638–3641. (g) Barbaro, P.; Bianchini, C.; Mealli, C.; Meli, A. *J. Am. Chem. Soc.* **1991**, *113*, 3181–3183. (h) Spartalian, K.; Carrano, C. J. *Inorg. Chem.* **1989**, *28*, 19–24.
- (13) Palaniandavar, M.; Mayilmurugan, R. *C. R. Chim.* **2007**, *10*, 366–379.

- (14) Ray, S.; Mohan, R.; Singh, J. K.; Samantaray, M. K.; Shaikh, M. M.; Panda, D.; Ghosh, P. *J. Am. Chem. Soc.* **2007**, *129*, 15042–15053.
- (15) John, A.; Shaikh, M. M.; Ghosh, P. *Dalton Trans.* **2008**, 2815–2824.
- (16) Viswanathan, R.; Palaniandavar, M.; Balasubramanian, T.; Muthiah, P. T. *J. Chem. Soc., Dalton Trans.* **1996**, 2519–2525.

Scheme 1



{[bis((1-methylimidazol-2-yl)methyl)amino]acetate}FeCl₂,¹⁷ showed charge-transfer bands at 332 nm ($\epsilon = 4620 \text{ M}^{-1} \text{ cm}^{-1}$) and 306 nm ($\epsilon = 5950 \text{ M}^{-1} \text{ cm}^{-1}$). In addition to the two charge-transfer bands, two more ligand based high energy transitions were observed at 213 nm and as a shoulder near ~ 258 nm (see Table S1 in the Supporting Information). The absorption at ~ 258 nm is attributed to the $\pi-\pi^*$ transition of the ligand.^{10e,16} Consistent with the high-spin d^5 configuration of the iron(III) center in the **1b**, **2b**, and **3b** complexes, no $d-d$ transitions were observed.

X-ray diffraction studies further confirmed the facial binding of the **1a**, **2a**, and **3a** ligands to the metal centers in the **1b**, **2b**, and **3b** complexes (see Figure 2 and Figures S1 and S2 and Table S2 in the Supporting Information). In particular, these complexes displayed a distorted octahedral geometry around the iron(III) center, with one triangular face of the octahedron capped by the respective chelating **1a**, **2a**, and **3a** ligands and the other diametrically opposite triangular face occupied by Cl atoms at its three vertices. In this regard, it is worth mentioning that the facial binding of the ligands in iron(III) model complexes has been reported to be an important prerequisite for designing synthetic models of catechol dioxygenase.¹³ For example, {[3,3-bis(1-ethyl-4-isopropylimidazol-2-yl)propionate]}iron(3,4,5,6-tetrachlorocatecholato)(H₂O), a high-spin octahedral iron(III)

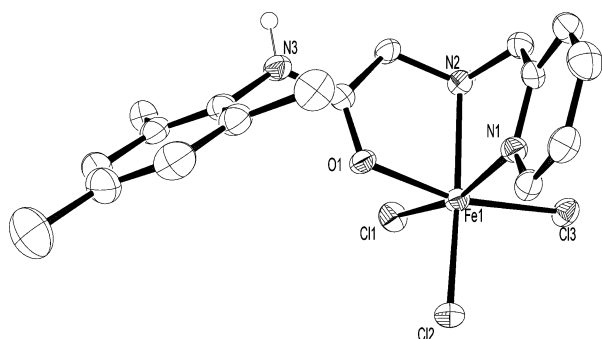


Figure 2. ORTEP drawing of **1b**. Selected bond lengths (\AA) and angles (deg): Fe1–O1 2.075(2), Fe1–N1 2.222(3), Fe1–N2 2.230(3), Fe1–Cl2 2.2808(11), Fe1–Cl1 2.3062(11), Fe1–Cl3 2.3214(10); O1–Fe1–N1 81.18(10), O1–Fe1–N2 77.80(10), N1–Fe1–N2 75.86(11), O1–Fe1–Cl2 92.16(7), N1–Fe1–Cl2 91.84(8), N2–Fe1–Cl2 165.07(8), O1–Fe1–Cl1 90.04(7), N1–Fe1–Cl1 164.45(8).

complex supported over a facially bound [N₂O] ligand, is reported to be an excellent model of catechol dioxygenase.^{12c}

Another important requirement of an intradiol catechol dioxygenase model is the high-spin nature of the iron(III) metal center. In this context, the electron paramagnetic resonance (EPR) studies of the **1b**, **2b**, and **3b** complexes deserve mention. In particular, the X-band EPR spectra of **1b**, **2b**, and **3b**, recorded in the frozen state in (CH₃)₂SO at 77 K, each showed a well-resolved signal at a g value [4.16 (**1b**), 4.14 (**2b**), and 4.16 (**3b**)] typical of a monomeric high-spin Fe(III) center in a distorted octahedral environment (Figure 3). For example, similar EPR spectra were observed for related monomeric high-spin octahedral complexes, namely, [bis(pyridin-2-ylmethyl)amine]FeCl₃¹⁶ ($g = 4.30$), [bis(benzimidazol-2-ylmethyl)amine]FeCl₃¹⁶ ($g = 4.22$), and [4,5-dichloro-1,2-bis(pyridinecarboxamido)benzene]Fe(NEt₄)Cl₂¹⁸ ($g = 4.28$).

In order to further determine the spin state of the **1b**, **2b**, and **3b** complexes and its dependence on temperature, the solid-state variable-temperature magnetic susceptibility experiments were performed in the temperature range 10–304 K (Figure S3 in the Supporting Information). The effective magnetic moments of the metal centers in **1b**, **2b**, and **3b** were determined to be 5.70, 5.56, and 5.89 μ_B , respectively, at 298 K and are consistent with the high-spin nature ($S = 5/2$) of the metal center in these complexes.¹⁹ It is worth noting that the high-spin state of the iron(III) center was found to remain constant over the whole temperature range except for a sharp decrease in the magnetic moment (μ_B) at 10 K, which may be ascribed to the strong antiferromagnetic exchange interaction between iron(III) centers.²⁰ In this regard, it is worth mentioning that a similar observation has been reported for a high-spin iron(III) complex bearing an

(17) Rodriguez, M. C.; Badarau, I. M.; Cesario, M.; Guilhem, J.; Keita, B.; Nadjjo, L. *Inorg. Chem.* **1996**, *35*, 7804–7810.

(18) Ray, M.; Mukherjee, R.; Richardson, J. F.; Buchanan, R. M. *J. Chem. Soc., Dalton Trans.* **1993**, 2451–2457.

(19) (a) Malfant, I.; Badarau, I. M.; Levisalles, M. P.; Lloret, F. *J. Chem. Soc., Chem. Commun.* **1990**, 1338–1340. (b) Burnett, M. G.; McKeel, V.; Nelson, S. M. *J. Chem. Soc., Dalton Trans.* **1981**, 1492–1497. (c) Reiff, W. M.; Baker, W. A., Jr.; Erickson, N. E. *J. Am. Chem. Soc.* **1968**, *90*, 4794–4800.

(20) Korendovych, I. V.; Staples, R. J.; Reiff, W. M.; Rybak-Akimova, E. V. *Inorg. Chem.* **2004**, *43*, 3930–3941.

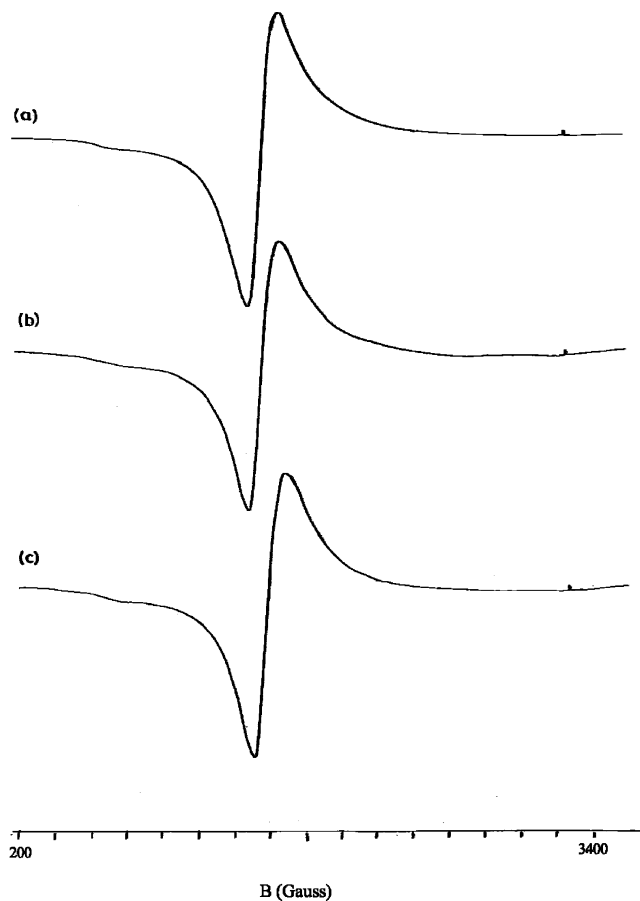


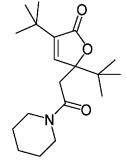
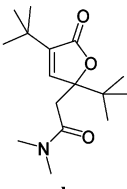
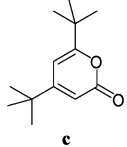
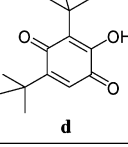
Figure 3. X-band EPR overlay spectra of the iron(III) complexes: (a) **1b** ($g = 4.16$), (b) **2b** ($g = 4.14$), and (c) **3b** ($g = 4.16$) in $(\text{CH}_3)_2\text{SO}$ at 77 K.

[NNN]-bound polyimidazole ligand.²¹ Furthermore, the temperature variations of inverse molar susceptibility ($1/\chi_M$) of the **1b**, **2b**, and **3b** complexes show linear increases with the temperature in accordance with the Curie–Weiss law for the same temperature range.

The Mössbauer spectra of **1b**, **2b**, and **3b** further confirm both the oxidation state (III+) and the high-spin state of the metal center in these complexes (Figure S4 in the Supporting Information). Specifically, the isomeric shift (δ) [0.33 mm s^{-1} (**1b**), 0.22 mm s^{-1} (**2b**), and 0.20 mm s^{-1} (**3b**)] and the quadrupole splitting (ΔE_Q) [0.30 mm s^{-1} (**1b**), 0.42 mm s^{-1} (**2b**), and negligible (**3b**)] are in good agreement with those reported for related high-spin iron(III) complexes.²² For example, a high-spin octahedral [N -(8-quinolyl)salicylaldimine] $_2\text{FeCl}_2^{23}$ complex showed a broad singlet with an isomeric shift (δ) of 0.25 mm s^{-1} and a quadrupole splitting (ΔE_Q) of 0.38 mm s^{-1} at 400 K.

Having unequivocally established the high-spin nature of the facially bound octahedral iron(III) complexes **1b**, **2b**, and

Table 1. Oxidative Cleavage Products of 3,5-Di-*tert*-butylcatechol by **1b**, **2b**, and **3b**

cleavage type	cleavage product	1b (%)	2b (%)	3b (%)
intradiol	 a	78	83	82
	 b	3	3	3
extradiol	 c	3	3	3
other	 d	7	4	7

3b, we proceeded to carry out the catalysis study. Indeed, as anticipated, all of the **1b**, **2b**, and **3b** complexes showed excellent highly regioselective intradiol cleavage activity toward the 3,5-di-*tert*-butylcatechol substrate in the presence of molecular oxygen at room temperature under ambient conditions (Table 1). Specifically, when 3,5-di-*tert*-butylcatechol was treated with each of the **1b**, **2b**, and **3b** complexes in *N,N*-dimethylformamide (DMF) in the presence of piperidine as a base and the resultant mixture was bubbled with molecular oxygen, the formation of highly regioselective intradiol products constituted of a *major* product **a** [78% (**1b**), 83% (**2b**), and 82% (**3b**)] and a *minor* product **b** [3% (**1b**), 3% (**2b**), and 3% (**3b**)] was observed. Interestingly enough, both of the intradiol products, **a** and **b**, originate from the same parent muconic anhydride derivative. Also, in keeping with the highly regioselective intradiol cleavage ability of the **1b**, **2b**, and **3b** complexes, very little formation of an extradiol product **c** [3% (**1b**), 3% (**2b**), and 3% (**3b**)], also identified by gas chromatography/mass spectrometry (GC/MS) analysis, was observed. In addition, a small amount of another product, identified as **d** [7% (**1b**), 4% (**2b**), and 7% (**3b**)], was also seen.

The nature of the product of the oxidative cleavage reaction, whether intradiol or extradiol, is determined by the identity of the migrating group during the course of 1,2-Criegee rearrangement⁷ (see Scheme S1 in the Supporting Information). Quite interestingly, an acyl migration during the 1,2-Criegee rearrangement step yields the muconic

(21) Chauvin, A. S.; Frapart, Y. M.; Vaissermann, J.; Donnadieu, B.; Tuchagus, J. P.; Chottard, J. C.; Li, Y. *Inorg. Chem.* **2003**, *42*, 1895–1900.

(22) (a) Brewer, C.; Brewer, G.; Butcher, R. J.; Carpenter, E. E.; Cuenca, L.; Noll, B. C.; Scheidt, W. R.; Viragh, C.; Zavali, P. Y.; Zielaski, D. *Dalton Trans.* **2006**, 1009–1019. (b) Maeda, Y.; Oshio, H.; Toriumi, K.; Takashima, Y. *J. Chem. Soc., Dalton. Trans.* **1991**, 1227–1235.

(23) Hayami, S.; Gu, Z. Z.; Yoshiki, H.; Fujishima, A.; Sato, O. *J. Am. Chem. Soc.* **2001**, *123*, 11644–11650.

anhydride derivative, which serves as a common precursor for all of the intradiol-cleaved products, while an alkenyl migration produces oxepine-2,3-dione, which serves as a precursor for all of the extradiol-cleaved products. Specifically, the intradiol products, **a** and **b**, are formed by the nucleophilic attack of piperidine and NH(Me)₂, an impurity in the DMF solvent, on the less hindered carbonyl group of the muconic anhydride followed by subsequent cyclization,^{9h,10c} while the extradiol cleavage product, **c**, is formed by the ring contraction of the parent-substituted oxepine-2,3-dione.^{7,9a}

It is worth noting that very little influence of the sterics due to the phenyl ring in **1b**, **2b**, and **3b** was observed because the product distribution remained almost unchanged upon increasing the phenyl ring sterics along **1b** to **2b** to **3b**, which suggests that the phenyl ring lies too far away from the metal center to exercise any tangible influence on the catalysis (see Table 1, Figure 2, and Figures S1 and S2 in the Supporting Information).

More importantly, the **1b**, **2b**, and **3b** complexes were found to exhibit superior regioselective intradiol catechol cleavage activity compared to many other known model complexes. For example, a recently reported synthetic analogue of catechol dioxygenase, namely, (pyridine-2,6-dicarboxylato)Fe^{III}Cl(H₂O)₂, exhibited much less selectivity of up to 57% in 48 h^{10c} toward the intradiol-cleaved products among an array of intradiol, extradiol, and other products that it produced upon reaction with the catechol substrate. Similarly, another small-molecule enzyme model, (2,6-bis-benzimidazolylpyridine)Fe^{III}Cl₃, showed extremely poor selectivity, producing only ca. 10% of the intradiol cleavage products in 48 h.^{10c} Other models, like [N,N-dimethyl-N'-(pyridin-2-ylmethyl)-N'-(2-oxy-4-nitrobenzyl)ethylenediamine]Fe^{III}Cl₂ and [N,N-dimethyl-N'-(1-methylimidazol-2-ylmethyl)-N'-(2-oxy-4-nitrobenzyl)ethylenediamine]Fe^{III}Cl₂, showed selectivity of up to 54% and 77%, respectively, for the intradiol products in 48 h.^{10e} However, a recently reported [N,N-dimethyl-N'-(2-oxy-3,5-dimethylbenzyl)-N'-(pyridin-2-ylmethyl)ethylenediamine]iron(III) (3,5-di-*tert*-butylcatecholate) complex showed excellent selectivity, up to 94%, toward the formation of the intradiol-cleaved products in 24 h.^{10b} Along similar lines, the [N,N'-dimethyl-N,N'-bis(4-chloro-2-pyridylmethyl)ethane-1,2-diamine]iron(III) (3,5-di-*tert*-butylcatecholate)(BPh₄) complex gave 90% intradiol-cleaved products in 48 h.²⁴ It is worth noting that most of these models showed a higher reaction time of 48 h as compared to 24 h exhibited by **1b**, **2b**, and **3b**. There also exist examples of model complexes requiring much longer reaction times, like the [methylbis(1-methylimidazol-2-yl)(2-oxyphenyl)methylether]iron(III)(3,5-di-*tert*-butylcatecholate) complex, supported over a facially bound anionic [NNO] ligand,^{12b} which showed selectivity of only 40% of the intradiol products after 2 weeks. In light of the above facts, quite significantly, the {[N-methyl-N,N',N''-tris(2-pyridylmethyl)ethane-1,2-diamine]}iron(III)(3,5-di-*tert*-butylcatecholate)(BPh₄) complex yielded 90% of the intradiol-

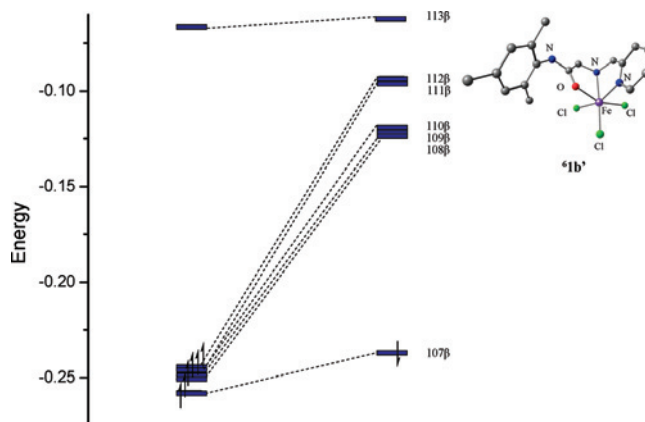


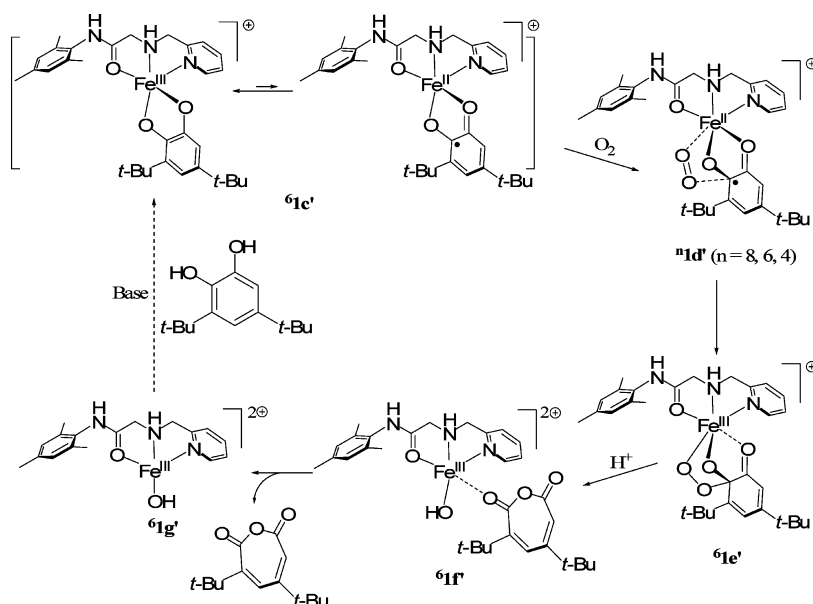
Figure 4. Frontier molecular orbitals of **1b'** (energy units are in hartrees).

cleaved products after a much shorter reaction time of 6 h.²⁴ Thus, because of their superior regioselectivity (ca. 81–85%) among the known synthetic models, the **1b**, **2b**, and **3b** complexes can be regarded as to quite closely emulate the native intradiol catechol dioxygenase enzyme, which exclusively gives the intradiol-cleaved products.

In order to obtain insight into the electronic structures of the iron(III) complexes (**1b**, **2b**, and **3b**), DFT studies were carried out. Specifically, the geometry-optimized structures, **1b'**, **2b'**, and **3b'**, of the respective **1b**, **2b**, and **3b** complexes were computed at the UB3LYP/LANL2DZ,6-31G(d) level of theory using the atomic coordinates adopted from X-ray analysis and, subsequently, single-point calculations were performed at the same level of theory for a detailed prediction of the electronic properties of these complexes. The optimized structures of the iron complexes (**1b'**, **2b'**, and **3b'**) exhibited a distorted octahedral geometry around the iron(III) center with facial ligand coordination similar to the X-ray structures (see Figure 4 and Figures S5–S7 and Tables S13–S15 in the Supporting Information). The computed metrical data were found to be in reasonable agreement with the X-ray structures, with the exception of the Fe–Cl bond distances, which were found to be unsymmetrical (see Tables S16–S18 in the Supporting Information). More significantly, the DFT studies unequivocally established the high-spin state of the iron complexes (**1b'**, **2b'**, and **3b'**) and corroborated the experimental findings discussed earlier (see Table S19 in the Supporting Information). In particular, the EPR peak at *g* values of 4.16 (**1b**), 4.14 (**2b**), and 4.16 (**3b**), the Mössbauer isomeric shift at 0.33 mm s⁻¹ (**1b**), 0.22 mm s⁻¹ (**2b**), and 0.20 mm s⁻¹ (**3b**) with the respective quadrupole splittings of 0.30 mm s⁻¹ (**1b**), 0.42 mm s⁻¹ (**2b**), and negligible (**3b**), and the magnetic susceptibility measurements of magnetic moments (μ_B) of 5.70 μ_B (**1b**), 5.56 μ_B (**2b**), and 5.89 μ_B (**3b**) at 298 K all point toward the high-spin nature of the **1b**, **2b**, and **3b** complexes. A careful scrutiny of the molecular orbitals of the computed **1b'**, **2b'**, and **3b'** complexes indeed revealed that five metal d orbitals in **1b'** (108 α –112 α), **2b'** (112 α –116 α), and **3b'** (120 α –124 α) were singly occupied with the corresponding vacancies lying in their respective β -spin orbitals in **1b'** (108 β –112 β), **2b'** (112 β –116 β), and

(24) Mialane, P.; Tchertanov, L.; Banse, F.; Sainion, J.; Girerd, J.-J. *Inorg. Chem.* **2000**, *39*, 2440–2444.

Scheme 2



3b' (120β – 124β) complexes (see Figure 4 and Figures S5–S7 in the Supporting Information).

The mechanistic studies of the catechol intradiol cleavage pathway on a representative mesityl derivative **1b'** were carried out based on a popularly proposed mechanism (Scheme 2).^{3,25} Specifically, each of the intermediates in the mechanistic pathway was computationally modeled from the starting **1b'** structure by appropriate modification of the metal-bound ligand moieties and then geometry-optimized. Subsequent single-point calculations were performed on the geometry-optimized structures for obtaining insight into the detailed electronic structure of each of the intermediates.

The first step in the proposed catalytic cycle involves the binding of the 3,5-di-*tert*-butylcatecholate moiety to the iron **1b'** complex as mimicked by cationic intermediate **1c'** (see Scheme 2 and Figure S8 and eq S1 in the Supporting Information). Quite significantly, the intermediate **1c'** exhibits substantial radical (semiquinonate) character similar to that observed in the catalytic cycle of the native enzyme (see Scheme 2 and Figure S9 in the Supporting Information). For example, the Fe–O bond lengths of **1c'** were found to be in reasonable agreement with the substrate (3,4-dihydroxybenzoate)-bound intradiol catechol dioxygenase (see Table S20 in the Supporting Information). Further evidence in favor of the semiquinonate character comes from the Mulliken spin-density analysis (see Tables S19 and S21 in the Supporting Information), which showed a decrease in the spin-density on the iron center upon catecholate binding and which arises from the reduction of the metal center from iron(III) in **1b'** to iron(II) in **1c'**. Specifically, the Mulliken spin-density on iron reduces from 3.91 (**1b'**) to 3.73 (**1c'**), while the catecholate ring acquires a net spin-density of 1.14 (**1c'**) (see Tables S19 and S21 in the Supporting Information).²⁵ Similarly, consistent with the iron(II) state of the metal center, the frontier molecular orbital diagram of **1c'**

showed five vacancies, four of which lie on metal-based orbitals (146β – 143β) while one is on the catechol-based (142β) molecular orbital (see Figure S9 and Table S22 in the Supporting Information). As expected, such vacancies (four metal-based and one catechol-based) are in stark contrast to the exclusive five metal-based orbitals seen in the precursor iron(III) **1b'** complexes. Furthermore, a closer look at the molecular orbitals showed the presence of σ interactions (135β and 137β orbitals) between the iron(II) center and the catecholate moiety, a σ^* interaction (142α orbital), and π interactions (136β , 141β , and 142β orbitals) (see Table S23 in the Supporting Information).

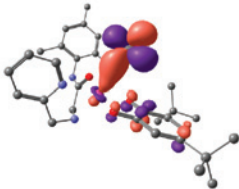
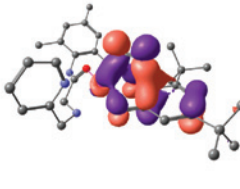
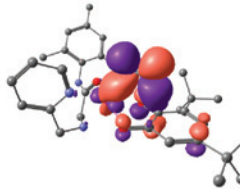
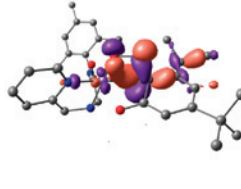
At this juncture, it is worth pointing out that the presence of the iron(II) semiquinonate character of the **1c'** intermediate is crucial for the dioxygen binding that happens in the subsequent step of the catalytic cycle.^{3a,26} Indeed, the attack on the **1c'** intermediate by the dioxygen molecule containing two unpaired electrons in its π^* orbitals (in a triplet ground state, $^3\text{O}_2$) can occur either at the iron center or at the catecholate radical site. The approach of the $^3\text{O}_2$ molecule to the **1c'** intermediate can lead to three possible spin states: **81d'** (both $^3\text{O}_2$ spins remain unpaired), **61d'** (one $^3\text{O}_2$ spin is paired), and **41d'** (both $^3\text{O}_2$ spins are paired) (see Scheme 2 and Figures S10–S12 in the Supporting Information). Of these three states, the lowest in energy is the **41d'** species, while **61d'** and **81d'** are higher by 1.5 and 5.7 kcal mol⁻¹, respectively, relative to the quartet species (**41d'**).²⁵

Interesting interactions of the $^3\text{O}_2$ molecule with the iron center and the catecholate ring are seen in these **81d'**, **61d'**, and **41d'** species. For example, a weak interaction is present between $^3\text{O}_2$ and the iron(II) center in **81d'** as evidenced by a Fe \cdots O=O' distance of 2.88 Å, which is larger than the

(25) Borowski, T.; Siegbahn, P. E. M. *J. Am. Chem. Soc.* **2006**, *128*, 12941–12953.

(26) (a) Horsman, G. P.; Jirasek, A.; Vaillancourt, F. H.; Barbosa, C. J.; Jarzecki, A. A.; Xu, C.; Mekmouche, Y.; Spiro, T. G.; Lipscomb, J. D.; Blades, M. W.; Turner, R. F. B.; Eltis, L. D. *J. Am. Chem. Soc.* **2005**, *127*, 16882–16891. (b) Funabiki, T.; Yamazaki, T. *J. Mol. Catal.* **1999**, *150*, 37–47.

Table 2. Molecular Orbitals Showing Significant Interactions between the Iron Center, the Catecholite Moiety, and Dioxygen in **⁸1d'**, **⁶1d'**, **⁴1d'**, and **⁶1e'**

⁸1d'	⁶1d'	⁴1d'	⁶1e'
			
149β	149β	150β	144β

sum of the covalent radii (2.02 Å) but smaller than the sum of the van der Waals radii (3.52 Å) of the individual atoms (see Figure S10 and Tables S24 and S25 in the Supporting Information). Remarkably enough, no interaction was, however, seen to occur between the catecholite radical and the dioxygen molecule, as seen by the long C···O'=O distance of 3.78 Å, which is larger than both the sum of the individual covalent radii (1.36 Å) and the van der Waals radii (3.22 Å). The parallel spin arrangement in **⁸1d'** is also reflected in the distribution of spin densities on the individual moieties (Fe = 3.73; catechol ring = 1.14; O₂ = 0.955 and 1.043) (see Table S21 in the Supporting Information). As expected, the frontier molecular orbital diagram of the intermediate **⁸1d'** species displayed seven vacancies in the spin β orbitals that comprised four iron(II) (152β–155β), one catecholite ring (151β), and two dioxygen (149β–150β) based molecular orbitals (see Figure S10 and Table S24 in the Supporting Information). The σ and π interactions between the iron center and the catecholite ion are seen in 142β, 144β and 148β, 151β molecular orbitals, respectively, while the σ* and π* interactions are in the 151α and 149α orbitals, respectively (see Table S25 in the Supporting Information). Of significance is the weak interaction of the d_{z²} orbital of the iron(II) center with the singly occupied π* orbital of the ³O₂ moiety present in the 149β orbital and as a consequence of which the O–O distance (1.214 Å) is slightly elongated compared to that of the free ³O₂ molecule (1.207 Å) (Table 2).

In stark contrast to the weak interaction observed between ³O₂ and the iron(II) center in the **⁸1d'** species, the lower energy **⁶1d'** species exhibits a significantly stronger interaction of ³O₂ with both the iron(II) center and the catecholite radical moiety, and this is apparent from the shorter Fe···O=O' (2.358 Å) and C···O'=O (2.493 Å) distances observed in the **⁶1d'** species compared to the **⁸1d'** species (see Figure S11 and Tables S26 and S27 in the Supporting Information). The spin-density analysis revealed a reduction in the spin-density on the catechol ring (–0.390) and the dioxygen moiety (0.829 and 0.729), indicating a spin-paired interaction between the two, while the net spin-density on the iron(II) center remained unchanged (3.70) and is indicative of a spin-parallel interaction with ³O₂ (see Table S21 in the Supporting Information). Further support in favor of the

spin-paired interaction between the catechol ring and the ³O₂ moiety in the **⁶1d'** species comes from the frontier molecular orbital diagram, which displays only five vacancies in the spin β orbitals (154β–150β), in contrast to seven vacancies in the **⁸1d'** species (see Figure S11 and Table S26 in the Supporting Information). The individual σ interactions of the iron(II) center with the ³O₂ moiety (iron(II) center–³O₂) and the catecholite ring with the ³O₂ moiety (catecholite ring–³O₂) are depicted by 150β and 148α orbitals, respectively, while the 151α orbital depicts the corresponding σ* interaction (see Table S27 in the Supporting Information). Of importance is the 149β orbital, which represents simultaneous σ interaction between the iron(II) center, the catecholite radical, and the ³O₂ moieties in the **⁶1d'** species (Table 2). A careful scrutiny reveals that a π* orbital of ³O₂ is simultaneously interacting with a d_{z²} orbital of the iron(II) center and a C–C π-bonding orbital of the catecholite ring in the 149β orbital. The spin-paired interaction of the catecholite ring with that of the ³O₂ results in further elongation of the O–O distance (1.255 Å) in the ³O₂ moiety.

The interaction of the ³O₂ moiety with the iron(II) center and the catecholite ring is most pronounced in the lowest energy **⁴1d'** species, which exhibits a much reduced Fe···O=O' (2.192 Å) distance, while the C···O'=O (2.529 Å) distance remains almost unchanged (see Figure S12 and Tables S28 and S29 in the Supporting Information). As anticipated, the net spin densities on the iron center (1.927), the catecholite ring (0.292), and the O₂ (0.396 and 0.363) moieties are drastically diminished (see Table S21 in the Supporting Information). The frontier molecular orbital diagram displays only three vacancies in the spin β orbitals (153β–151β), thereby indicating a spin-paired interaction of the ³O₂ moiety with both the iron(II) center and catecholite ring (see Figure S12 and Table S28 in the Supporting Information). The σ interactions of the ³O₂ moiety with the iron(II) center and the catecholite ring are seen in 146β, 147α, and 147β orbitals, while the π interaction is seen in the 152β orbital (see Table S29 in the Supporting Information). Additionally, the 150β orbital displays the simultaneous interaction of the dioxygen π* orbital with a d orbital of the iron(II) center and the catecholite ring (Table 2). The O–O bond distance (1.257 Å) is, however, comparable to that observed in the **⁶1d'** species.

Of these ternary species ($^8\mathbf{1d}'$, $^6\mathbf{1d}'$, and $^4\mathbf{1d}'$), involving the iron(II) center, the catecholate radical, and the bound dioxygen moiety, further progress of the reaction proceeds via the sextet $^6\mathbf{1d}'$ species, which is energetically accessible from both the $^8\mathbf{1d}'$ and $^4\mathbf{1d}'$ species. Specifically, the interaction of the sextet $^6\mathbf{1c}'$ with $^3\text{O}_2$ leads to the quartet $^4\mathbf{1d}'$ as well as the octet $^8\mathbf{1d}'$ spin states, which upon intersystem crossing (endothermic by $1.5 \text{ kcal mol}^{-1}$ for the $^4\mathbf{1d}'$ species and exothermic by $4.2 \text{ kcal mol}^{-1}$ for the $^8\mathbf{1d}'$ species) gives rise to the sextet spin state $^6\mathbf{1d}'$ from which the subsequent catalytic cycle proceeds. A similar observation has been reported by Borowski and Siegbahn²⁵ when the catalytically active sextet spin state was accessed by an analogous intersystem crossing from the quartet and octet states (both endothermic by 7 kcal mol^{-1}). The $^6\mathbf{1d}'$ species yields the alkylperoxoiron(III) intermediate, $^6\mathbf{1e}'$, which undergoes a 1,2-Criegee-type rearrangement, giving rise to the final iron(III)-bound muconic anhydride derivative ($^6\mathbf{1f}'$), which on subsequent hydrolysis yields acyclic end products (see Scheme S1 in the Supporting Information). Specifically, the 1,2-Criegee-type rearrangement⁷ involves a homolytic O–O bond cleavage with a simultaneous acyl group migration, resulting in the muconic anhydride intermediate.

The geometry-optimized structure of the $^6\mathbf{1e}'$ species exhibits not only significantly reduced Fe \cdots O–O' (1.786 Å) and C \cdots O'–O (1.458 Å) bond lengths but also an appreciably elongated O–O' (1.445 Å) bond length, thereby attesting to its peroxo (O_2^{2-}) nature (see Figure S13 and Tables S30–S31 in the Supporting Information). Both the net spin densities [Fe (3.93), catechol ring (0.367), and O_2 (0.094 and 0.407)] (see Table S21 in the Supporting Information) and five vacant spin β orbitals (150β – 154β) (see Figure S13 and Table S30 in the Supporting Information) support the peroxo nature of the $^6\mathbf{1e}'$ species and also indicate the concomitant oxidation of the iron(II) center in the precursor $^6\mathbf{1d}'$ species to the iron(III) center in the peroxo $^6\mathbf{1e}'$ species. Furthermore, it is worth mentioning that the C33–O2 bond is shortened (from 1.276 to 1.251 Å) and the corresponding Fe–O bond is markedly elongated (from 2.048 to 2.238 Å), similar to that seen in the enzyme active site.²⁵ The σ interaction of the peroxo moiety with the iron(III) center and the catechol ring in the $^6\mathbf{1e}'$ species occurs in the 151β orbital, while the π interactions occur in the 146β and 147β orbitals (see Figure S13 and Table S31 in the Supporting Information). Lastly, the 144β and 145β orbitals represent the simultaneous σ and π interactions, respectively, between the peroxo moiety, the iron(III) center and the catechol ring in the $^6\mathbf{1e}'$ species (Table 2).

The iron(III)-bound muconic anhydride derivative ($^6\mathbf{1f}'$) showed a Fe \cdots O bond of 2.024 Å, which is in close agreement with the sum of their covalent radii (2.02 Å) (see Figure S14 and Table S32 in the Supporting Information). As expected, the Mulliken spin-density analysis revealed an enhanced net spin-density on the iron center (4.01), indicating the presence of an iron(III) center arising out of the 1,2-Criegee-type rearrangement (see Table S21 in the Supporting Information). Additionally, the frontier molecular orbital diagram displays five vacancies in the spin β orbitals

(154β – 150β) located on the iron center, also validating its high-spin iron(III) nature (see Figure S14 and Table S32 in the Supporting Information).

In the subsequent step of the catalytic cycle, the weakly bound muconic anhydride derivative is released from the $^6\mathbf{1f}'$ species, resulting in the Fe^{III}OH intermediate $^6\mathbf{1g}'$, which can again enter the catalytic cycle upon reaction with a 3,5-di-*tert*-butylcatecholate dianion (see Scheme 2 and Figure S15 and Table S33 in the Supporting Information). It is worth noting that the O atom of the [Fe^{III}OH] moiety in the $^6\mathbf{1g}'$ species originates from the peroxo fragment of the $^6\mathbf{1e}'$ species as a consequence of the 1,2-Criegee rearrangement. Consistent with the high-spin iron(III) metal center, the spin-density analysis showed a residual spin of 3.84 on the metal center (see Figure S16 and Table S21 in the Supporting Information). Further orbital analysis also revealed the presence of five iron-based vacancies (90β – 86β) in the spin β orbitals (see Figure S15 and Table S33 in the Supporting Information).

It is worth pointing out the similarities that exist between the computed intermediates and those reported for the real mechanism. For example, the binding of the catecholate substrate to the metal center, resulting in the semiquinonate character,^{9c,e,27} has been appropriately modeled in the $^6\mathbf{1c}'$ species, which clearly reveals the semiquinonate character of the catechol ring, as had been observed experimentally. It is worth noting that the semiquinonate species is important particularly with respect to binding of $^3\text{O}_2$ in the subsequent step, which has been successfully modeled in three spin states, $^8\mathbf{1d}'$, $^6\mathbf{1d}'$, and $^4\mathbf{1d}'$. Additionally, the transient-metal-bound peroxo intermediate^{27–29} was also mimicked by the $^6\mathbf{1e}'$ species. Overall, a deeper insight into the enzyme mechanism could be obtained by looking into each of the computationally modeled intermediates, $^6\mathbf{1c}'$, $^8\mathbf{1d}'$, $^6\mathbf{1d}'$, $^4\mathbf{1d}'$, $^6\mathbf{1e}'$, $^6\mathbf{1f}'$, and $^6\mathbf{1g}'$.

Conclusion

In summary, a series of high-spin iron(III) complexes, **1b**, **2b**, and **3b**, supported over a new class of a facially binding [N_2O] ligand, provided an excellent synthetic mimic for the intradiol catechol dioxygenase enzyme by efficiently carrying out the oxidative intradiol cleavage of the 3,5-di-*tert*-butylcatechol substrate using molecular oxygen at room temperature under ambient conditions in a highly regiospecific manner. The DFT studies suggest that the oxidative cleavage of the catechol proceeds via an iron(III) peroxo intermediate analogous to that reported for the native enzyme.

Experimental Section

General Procedures. All manipulations were carried out using standard Schlenk techniques. Solvents were purified and degassed by standard procedures. 2,6-Diisopropylaniline, 2,6-diethylaniline, 2,4,6-trimethylaniline, and 2-picolylamine were purchased from

(27) Que, L., Jr.; Lipscomb, J. D.; Münck, E.; Wood, J. M. *Biochim. Biophys. Acta* **1977**, *485*, 60–74.

(28) Fujisawa, H.; Hiromi, K.; Uyeda, M.; Okuno, S.; Nozaki, M.; Hayaishi, O. *J. Biol. Chem.* **1972**, *247*, 4422–4428.

(29) Que, L., Jr.; Lipscomb, J. D.; Zimmermann, R.; Münck, E.; Orme-Johnson, N. R.; Orme-Johnson, W. H. *Biochim. Biophys. Acta* **1976**, *452*, 320–334.

Sigma Aldrich, Germany, chloroacetyl chloride was purchased from Spectrochem, India, and these were used without any further purification. 2-Chloro-*N*-(2,6-diisopropylphenyl)acetamide, 2-chloro-*N*-(2,6-diethylphenyl)acetamide, and 2-chloro-*N*-(2,4,6-trimethylphenyl)acetamide were prepared by the modified procedure reported in the literature.³⁰ ¹H and ¹³C{¹H} NMR spectra were recorded on a Varian 400 MHz NMR spectrometer. ¹H NMR peaks are labeled as singlet (s), doublet (d), triplet (t), and septuplet (sept). IR spectra were recorded on a Perkin-Elmer Spectrum One FT-IR spectrometer. Mass spectrometry measurements were done on a Micromass Q-ToF spectrometer. X-ray diffraction data were collected on a Bruker P4 diffractometer equipped with a SMART CCD detector, and crystal data collection and refinement parameters are summarized in Table S2 in the Supporting Information. The structures were solved using direct methods and standard difference map techniques and were refined by full-matrix least-squares procedures on *F*² with *SHELXTL* (version 6.10).³¹ The EPR measurements were made with a Varian model 109C E-line X-band spectrometer fitted with a quartz Dewar for measurements at 77 K. The spectra were calibrated by using tetracyanoethylene (*g* = 2.0037). The electronic spectra were recorded in CH₃CN by using a Jasco V-570 UV-vis spectrophotometer. The magnetization measurements were carried out as a function of the temperature and magnetic field using a vibrating sample magnetometer (Quantum Design) in the field-cooled mode. GC spectra were measured on a Shimadzu gas chromatograph GC-14A equipped with a flame ionization detector. Elemental analysis was carried out on Thermo Quest FLASH 1112 Series (CHNS) elemental analyzer.

Synthesis of *N*-(2,4,6-Trimethylphenyl)-2-[(pyridin-2-ylmethyl)amino]acetamide (1a). A mixture of 2-chloro-*N*-(2,4,6-trimethylphenyl)acetamide (2.00 g, 9.46 mmol), 2-picolylamine (1.54 g, 14.3 mmol), and K₂CO₃ (3.28 g, 23.7 mmol) in CH₃CN (ca. 40 mL) was refluxed with stirring for 30 h. The reaction mixture was cooled to room temperature and filtered and the filtrate concentrated under vacuum. The residue obtained was dissolved in CH₂Cl₂ (ca. 40 mL) and was washed with water (ca. 4 × 20 mL), after which the organic layer was separated, dried over anhydrous MgSO₄, and filtered. The filtrate was further concentrated under vacuum, washed with hot hexane (2 × 10 mL), and then vacuum-dried to obtain product **1a** as a viscous oil (2.01 g, 75%). ¹H NMR (CDCl₃, 400 MHz, 25 °C): δ 8.81 (s, 1H, NHCO), 8.58 (d, 1H, ³J_{HH} = 8 Hz, *o*-C₅H₄N), 7.66 (t, 1H, ³J_{HH} = 8 Hz, *p*-C₅H₄N), 7.25 (d, 1H, ³J_{HH} = 8 Hz, *m*-C₅H₄N), 7.20 (t, 1H, ³J_{HH} = 8 Hz, *m*-C₅H₄N), 6.87 (s, 2H, *m*-2,4,6-C₆H₂(CH₃)₃), 4.01 (s, 2H, COCH₂), 3.49 (s, 2H, CH₂C₅H₄N), 2.27 (s, 3H, *p*-2,4,6-C₆H₂(CH₃)₃), 2.18 (s, 6H, *o*-2,4,6-C₆H₂(CH₃)₃). ¹³C{¹H} NMR (CDCl₃, 100 MHz, 25 °C): δ 170.1 (NHCO), 158.3 (*ipso*-C₅H₄N), 149.4 (*o*-C₅H₄N), 136.6 (*p*-C₅H₄N), 134.7 (*ipso*-2,4,6-C₆H₂(CH₃)₃), 131.0 (*p*-2,4,6-C₆H₂(CH₃)₃), 128.7 (*m*- and *o*-2,4,6-C₆H₂(CH₃)₃), 122.3 (*m*-C₅H₄N), 122.2 (*m*-C₅H₄N), 54.9 (COCH₂), 52.1 (CH₂C₅H₄N), 20.8 (*p*-2,4,6-C₆H₂(CH₃)₃), 18.3 (*o*-2,4,6-C₆H₂(CH₃)₃). IR data (cm⁻¹, KBr pellet): 3850 (w), 3457 (br), 3249 (m), 3014 (m), 2917 (m), 2852 (m), 2130 (br), 1661 (s, ν_{CO}), 1589 (m), 1569 (w), 1522 (m), 1486 (m), 1431 (w), 1411 (w), 1309 (w), 1238 (m), 1145 (w), 1037 (w), 1015 (w), 994 (w), 965 (w), 848 (m), 754 (m), 720 (m), 601 (w), 553 (w), 524 (w). HRMS (ES). Calcd. for (M + H)⁺: *m/z* 284.1763. Found: *m/z* 284.1773.

Synthesis of {*N*-(2,4,6-Trimethylphenyl)-2-[(pyridin-2-ylmethyl)amino]acetamide}FeCl₃ (1b). To a solution of **1a** (0.853 g, 3.01 mmol) in dry CH₃OH (ca. 10 mL) was added FeCl₃ (0.491 g, 3.02 mmol), and the resulting solution was allowed to stir at room temperature, when a yellow precipitate appeared within a few minutes. The reaction mixture was further allowed to stir at room temperature for 2 h. The yellow precipitate was filtered and then washed with CH₂Cl₂ (3 × 10 mL) until the color of the washing changed from brown to yellow. It was further washed with cold CH₃OH (2 × 10 mL) and then vacuum-dried to obtain product **1b** as a yellow powdery solid (1.02 g, 76%). IR data (cm⁻¹, KBr pellet): 3548 (w), 3258 (m), 3089 (w), 2922 (w), 1623 (s, ν_{CO}), 1605 (s), 1558 (m), 1484 (w), 1429 (w), 1384 (w), 1342 (w), 1303 (w), 1277 (w), 1219 (w), 1156 (w), 1098 (w), 1021 (w), 1005 (m), 971 (w), 917 (w), 849 (w), 758 (m), 708 (m), 639 (w), 543 (w), 477 (w). UV-vis [CH₃CN, 1 × 10⁻⁴ M; λ_{max}, nm (ε, M⁻¹ cm⁻¹): 213 (20 859), 258 (9197), 298 (4827), 371 (3227). Magnetic moment (faraday balance): μ(298 K) = 5.70 μ_B. Anal. Calcd for C₁₇H₂₁Cl₃FeN₃O: C, 45.82; H, 4.75; N, 9.43. Found: C, 45.54; H, 5.02; N, 8.81.

Synthesis of *N*-(2,6-Diethylphenyl)-2-[(pyridin-2-ylmethyl)amino]acetamide (2a). A mixture of 2-chloro-*N*-(2,6-diethylphenyl)acetamide (2.50 g, 11.1 mmol), 2-picolylamine (1.79 g, 16.6 mmol), and K₂CO₃ (3.83 g, 27.7 mmol) in CH₃CN (ca. 40 mL) was refluxed with stirring for 30 h. The reaction mixture was cooled to room temperature and filtered and the filtrate concentrated under vacuum. The residue obtained was dissolved in CH₂Cl₂ (ca. 50 mL) and was washed with water (ca. 4 × 20 mL), after which the organic layer was separated, dried over anhydrous MgSO₄, and filtered. The filtrate was further concentrated under vacuum, washed with hot hexane (2 × 10 mL), and then vacuum-dried to obtain product **2a** as a brown viscous oil (2.25 g, 68%). ¹H NMR (CDCl₃, 400 MHz, 25 °C): δ 8.96 (s, 1H, NHCO), 8.58 (d, 1H, ³J_{HH} = 8 Hz, *o*-C₅H₄N), 7.67 (t, 1H, ³J_{HH} = 8 Hz, *p*-C₅H₄N), 7.26–7.19 (m, 3H, *p*-C₆H₃(CH₂CH₃)₂ and *m*-C₅H₄N), 7.12 (d, 2H, ³J_{HH} = 8 Hz, *m*-C₆H₃(CH₂CH₃)₂), 4.03 (s, 2H, COCH₂), 3.52 (s, 2H, CH₂C₅H₄N), 2.59 (q, 4H, ³J_{HH} = 8 Hz, C₆H₃(CH₂CH₃)₂), 1.19 (t, 6H, ³J_{HH} = 8 Hz, C₆H₃(CH₂CH₃)₂). ¹³C{¹H} NMR (CDCl₃, 100 MHz, 25 °C): δ 170.6 (NHCO), 158.2 (*ipso*-C₅H₄N), 149.2 (*o*-C₅H₄N), 141.0 (*ipso*-C₆H₃(CH₂CH₃)₂), 136.4 (*p*-C₅H₄N), 132.4 (*p*-C₆H₃(CH₂CH₃)₂), 127.4 (*o*-C₆H₃(CH₂CH₃)₂), 126.0 (*m*-C₆H₃(CH₂CH₃)₂), 122.1 (*m*-C₅H₄N), 121.9 (*m*-C₅H₄N), 54.8 (COCH₂), 52.0 (CH₂C₅H₄N), 24.6 (C₆H₃(CH₂CH₃)₂), 14.2 (C₆H₃(CH₂CH₃)₂). IR data (cm⁻¹, KBr pellet): 3856 (w), 3649 (w), 3480 (w), 3271 (w), 2956 (s), 2870 (s), 2041 (w), 1667 (s, ν_{CO}), 1591 (m), 1570 (w), 1495 (m), 1462 (s), 1377 (m), 1270 (w), 1221 (w), 1148 (w), 1131 (w), 1049 (w), 995 (w), 957 (w), 865 (w), 808 (w), 757 (m), 723 (m), 617 (w). HRMS (ES). Calcd for (M + H)⁺: *m/z* 298.1919. Found: *m/z* 298.1915.

Synthesis of {*N*-(2,6-diethylphenyl)-2-[(pyridin-2-ylmethyl)amino]acetamide}FeCl₃ (2b). To a solution of **2a** (0.608 g, 2.04 mmol) in dry CH₃OH (ca. 10 mL) was added FeCl₃ (0.331 g, 2.04 mmol), and the resulting solution was allowed to stir at room temperature, when a yellow precipitate appeared within a few minutes. The reaction mixture was further allowed to stir at room temperature for 2 h. The yellow precipitate was filtered and then washed with CH₂Cl₂ (3 × 10 mL) until the color of the washing changed from brown to yellow. It was further washed with cold CH₃OH (2 × 10 mL) and then vacuum-dried to obtain product **2b** as a yellow powdery solid (0.835 g, 89%). IR data (cm⁻¹, KBr pellet): 3504 (w), 3217 (m), 3075 (w), 2971 (m), 2933 (w), 1623 (s, ν_{CO}), 1583 (m), 1551 (m), 1486 (w), 1471 (m), 1456 (w), 1437 (m), 1381 (w), 1345 (w), 1305 (w), 1276 (w), 1239 (w), 1160 (w),

(30) Dave, M. P.; Patel, J. M.; Langalia, N. A.; Shah, S. R.; Thaker, K. A. *J. Indian Chem. Soc.* **1985**, *LXII*, 386–387.

(31) (a) Sheldrick, G. M. *SHELXL-97, Program for Refinement of Crystal Structures*; University of Göttingen: Göttingen, Germany, 1997. (b) Sheldrick, G. M. *SHELXS-97, Structure Solving Program*; University of Göttingen: Göttingen, Germany, 1997.

1099 (w), 1067 (w), 1022 (w), 1011 (m), 964 (w), 919 (w), 814 (w), 760 (m), 728 (m), 640 (w), 526 (w), 472 (w). UV-vis [CH_3CN , 1×10^{-4} M; λ_{max} , nm (ϵ , $\text{M}^{-1} \text{cm}^{-1}$): 213 (20 437), 258 (9021), 295 (4939), 371 (3490). Magnetic moment (faraday balance): $\mu(298 \text{ K}) = 5.56 \mu_{\text{B}}$. Anal. Calcd for $\text{C}_{18}\text{H}_{23}\text{Cl}_3\text{FeN}_3\text{O}$: C, 47.04; H, 5.04; N, 9.14. Found: C, 47.34; H, 5.29; N, 8.69.

Synthesis of *N*-(2,6-Diisopropylphenyl)-2-[(pyridin-2-ylmethyl)amino]acetamide (3a). A mixture of 2-chloro-*N*-(2,6-diisopropylphenyl)acetamide (2.01 g, 7.92 mmol), 2-picolylamine (1.28 g, 11.8 mmol), and K_2CO_3 (2.72 g, 19.7 mmol) in CH_3CN (ca. 40 mL) was refluxed with stirring for 30 h. The reaction mixture was cooled to room temperature and filtered and the filtrate concentrated under vacuum. The residue obtained was dissolved in CH_2Cl_2 (ca. 30 mL) and was washed with water (ca. 4×20 mL), after which the organic layer was separated, dried over anhydrous MgSO_4 , and filtered. The filtrate was further concentrated under vacuum, washed with hot hexane (2×10 mL), and then vacuum-dried to obtain product **3a** as a brown viscous oil (1.55 g, 60%). $^1\text{H NMR}$ (CDCl_3 , 400 MHz, 25 °C): δ 8.92 (s, 1H, *NHCO*), 8.59 (d, 1H, $^3J_{\text{HH}} = 8$ Hz, *o*- $\text{C}_5\text{H}_4\text{N}$), 7.67 (t, 1H, $^3J_{\text{HH}} = 8$ Hz, *p*- $\text{C}_5\text{H}_4\text{N}$), 7.31–7.20 (m, 3H, *p*- $\text{C}_6\text{H}_3(\text{CH}(\text{CH}_3)_2)$ and *m*- $\text{C}_5\text{H}_4\text{N}$), 7.18 (d, 2H, $^3J_{\text{HH}} = 8$ Hz, *m*- $\text{C}_6\text{H}_3(\text{CH}(\text{CH}_3)_2)$), 4.04 (s, 2H, COCH_2), 3.54 (s, 2H, $\text{CH}_2\text{C}_5\text{H}_4\text{N}$), 3.05 (sept, 2H, $^3J_{\text{HH}} = 7$ Hz, $\text{C}_6\text{H}_3(\text{CH}(\text{CH}_3)_2)$), 1.20 (d, 12H, $^3J_{\text{HH}} = 7$ Hz, $\text{C}_6\text{H}_3(\text{CH}(\text{CH}_3)_2)$). $^{13}\text{C}\{^1\text{H}\}$ NMR (CDCl_3 , 100 MHz, 25 °C): δ 170.9 (*NHCO*), 158.3 (*ipso*- $\text{C}_5\text{H}_4\text{N}$), 149.3 (*o*- $\text{C}_5\text{H}_4\text{N}$), 145.7 (*ipso*- $\text{C}_6\text{H}_3(\text{CH}(\text{CH}_3)_2)$), 136.4 (*p*- $\text{C}_5\text{H}_4\text{N}$), 131.1 (*p*- $\text{C}_6\text{H}_3(\text{CH}(\text{CH}_3)_2)$), 127.8 (*o*- $\text{C}_6\text{H}_3(\text{CH}(\text{CH}_3)_2)$), 123.2 (*m*- $\text{C}_6\text{H}_3(\text{CH}(\text{CH}_3)_2)$), 122.1 (*m*- $\text{C}_5\text{H}_4\text{N}$), 121.9 (*m*- $\text{C}_5\text{H}_4\text{N}$), 55.0 (COCH_2), 52.2 ($\text{CH}_2\text{C}_5\text{H}_4\text{N}$), 28.6 ($\text{C}_6\text{H}_3(\text{CH}(\text{CH}_3)_2)$), 23.4 ($\text{C}_6\text{H}_3(\text{CH}(\text{CH}_3)_2)$). IR data (cm^{-1} , KBr pellet): 3848 (w), 3467 (w), 3332 (m), 3286 (m), 3081 (m), 2969 (m), 2956 (m), 2924 (m), 2866 (m), 2250 (w), 1677 (s, ν_{CO}), 1589 (m), 1569 (w), 1501 (s), 1471 (m), 1435 (m), 1387 (w), 1358 (w), 1328 (w), 1276 (w), 1255 (w), 1125 (w), 1056 (w), 1019 (w), 934 (w), 891 (w), 872 (w), 798 (m), 751 (m), 672 (w), 511 (w), 493 (w). HRMS (ES). Calcd for $(\text{M} + \text{H})^+$: m/z 326.2232. Found: m/z 326.2223.

Synthesis of *N*-(2,6-Diisopropylphenyl)-2-[(pyridin-2-ylmethyl)amino]acetamide}FeCl₃ (3b). To a solution of **3a** (0.553 g, 1.70 mmol) in dry CH_3OH (ca. 10 mL) was added FeCl_3 (0.273 g, 1.68 mmol), and the resulting solution was allowed to stir at room temperature, when a yellow precipitate appeared within a few minutes. The reaction mixture was further allowed to stir at room temperature for 2 h. The yellow precipitate was filtered and then washed with CH_2Cl_2 (3×10 mL) until the color of the washing changed from brown to yellow. It was further washed with cold CH_3OH (2×10 mL) and then vacuum-dried to obtain product **3b** as a yellow powdery solid (0.628 g, 77%). IR data (cm^{-1} , KBr pellet): 3526 (w), 3248 (m), 3071 (w), 2967 (m), 2927 (w), 2868 (w), 1627 (s, ν_{CO}), 1609 (s), 1586 (m), 1475 (w), 1441 (w), 1382 (w), 1350 (w), 1281 (w), 1257 (w), 1157 (w), 1105 (w), 1054 (w), 1020 (w), 1005 (w), 974 (w), 922 (w), 798 (w), 768 (m), 726 (m), 640 (w), 521 (w), 474 (w). UV-vis [CH_3CN , 1×10^{-4} M; λ_{max} , nm (ϵ , $\text{M}^{-1}\text{cm}^{-1}$): 213 (20 657), 257 (9120), 293 (4935), 367 (3759). Magnetic moment (faraday balance): $\mu(298 \text{ K}) = 5.89 \mu_{\text{B}}$. Anal. Calcd for $\text{C}_{20}\text{H}_{27}\text{Cl}_3\text{FeN}_3\text{O}$: C, 49.26; H, 5.58; N, 8.62. Found: C, 48.92; H, 5.64; N, 8.39.

General Procedure for the Catechol Cleavage Activity. To a pretreated solution of 3,5-di-*tert*-butylcatechol (0.023 g, 0.103

mmol) and piperidine (0.018 g, 0.212 mmol) in 7 mL of DMF was added **1b**, **2b**, or **3b** (0.103 mmol), and oxygen was bubbled through the solution while stirring at room temperature for 24 h. The reaction was quenched by the addition of a 6 M HCl solution (ca. 25 mL), and the organic products were extracted from the aqueous solution with CHCl_3 (ca. 40 mL). The clear yellow CHCl_3 layer was separated and dried over anhydrous MgSO_4 . The solvent was concentrated to ca. 1 mL under reduced pressure. The products in the solution were quantified by GC (Shimadzu 14A) and subsequently identified by the GC/MS analysis. The products of dioxygenation of 3,5-di-*tert*-butylcatechol by the **1b**, **2b**, or **3b** complexes were identified by a modified procedure reported in the literature.^{9a,10b,d,f,32}

Computational Methods. DFT calculations were performed using the *Gaussian 03*³³ suite of quantum chemical programs on the **1b**, **2b**, and **3b** complexes and on its derived intermediates, **61c'**, **81d'**, **61d'**, **41d'**, **61e'**, **61f'**, and **61g'**, pertaining to a mechanistic pathway.^{3,25} The Becke three-parameter exchange functional in conjunction with the Lee–Yang–Parr correlation functional (B3LYP) has been employed in the study.³⁴ The LANL2DZ basis set was used for the Fe atom, while the 6-31G(d) basis set was used for all other atoms. Stationary-point calculations were carried out using the output coordinates from the geometry optimization calculations. Natural bond orbital (NBO) analysis³⁵ was performed using the *NBO 3.1* program implemented in the *Gaussian 03* package.

Acknowledgment. We thank DST, New Delhi, India, for financial support of this research. We are grateful to the National Single Crystal X-ray Diffraction Facility and Sophisticated Analytical Instrument Facility at IIT Bombay for the crystallographic and other characterization data. Computational facilities from the IIT Bombay Computer Center are gratefully acknowledged. The Mössbauer experiments were performed at the UGC-DAE Consortium for Scientific Research, Kolkata Centre. We thank Dr. D. Das for help with the Mössbauer experiments. The magnetic measurements were carried out at the Physical Property Measurement System (PPMS) Facility, Department of Physics, IIT Bombay. M.K.P. and A.J. thank CSIR, New Delhi, India, for a research fellowship.

Supporting Information Available: CIF file giving crystallographic data for **1b**, **2b**, and **3b**, ORTEP plots of **2b** and **3b**, variable-temperature magnetic susceptibility and Mössbauer plots, the B3LYP coordinates of the optimized geometries for **61b'**, **62b'**, **63b'**, **61c'**, **81d'**, **61d'**, **41d'**, **61e'**, **61f'**, and **61g'** along with the comparison tables, a spin-density table, frontier molecular orbital diagrams, electronic spectroscopic data, and complete ref 33. This material is available free of charge via the Internet at <http://pubs.acs.org>.

IC801576F

- (32) (a) Yoon, S.; Lee, H. J.; Lee, K.-B.; Jang, H. G. *Bull. Korean Chem. Soc.* **2000**, *21*, 923–928. (b) Ito, M.; Que, L., Jr. *Angew. Chem., Int. Ed.* **1997**, *36*, 1342–1344.
 (33) Frish, M. J.; et al. *Gaussian 03*, revision C.02; Gaussian, Inc.: Wallingford, CT, 2004.
 (34) (a) Becke, A. D. *Phys. Rev. A* **1988**, *38*, 3098–3100. (b) Lee, C.; Yang, W.; Parr, R. G. *Phys. Rev. B* **1988**, *37*, 785–789.
 (35) Reed, A. E.; Curtiss, L. A.; Weinhold, F. *Chem. Rev.* **1988**, *88*, 899–926.